Check for updates

AGU ADVANCING EARTH AND SPACE SCIENCES

JGR Solid Earth

RESEARCH ARTICLE

10.1029/2024JB028823

The Thermal Conductivity of Bridgmanite at Lower Mantle Conditions Using a Multi-Technique Approach

Eric Edmund[1], Irina Chuvashova[1,2], Zuzana Konôpková[3], Rachel Husband[4], Cornelius Strohm[4], Karen Appel[3], Carsten Bähtz[3,5], Orianna Ball[6], Victorien Bouffetier[3], Kara Brugman[1,7], Khachiwan Buakor[3], Julien Chantel[8], Stella Chariton[9], Matthew Duff[6], Anand Dwivedi[3], Konstantin Glazyrin[4], S. M. A. Hosseini-Saber[4], Nicolas Jaisle[10], Torsten Laurus[4], Xiang Li[11], Bernhard Masani[6], James McHardy[6], Malcolm McMahon[6], Sébastien Merkel[8], Katharina Mohrbach[4,11], Anshuman Mondal[4,11], Guillaume Morard[10], Vitali B. Prakapenka[9], Clemens Prescher[12], Young-Jay Ryu[9], Jan-Patrick Schwinkendorf[3], Minxue Tang[4], Zena Younes[6], Carmen Sanchez-Valle[11], Hanns-Peter Liermann[4], James Badro[13], Jung-Fu Lin[14], R. Stewart McWilliams[6], and Alexander F. Goncharov[1]

[1]Carnegie Science, Earth and Planets Laboratory, Washington, DC, USA, [2]Now at Florida International University, Miami, FL, USA, [3]European XFEL GmbH, Schenefeld, Germany, [4]Deutsches Elektronen-Synchrotron DESY, Hamburg, Germany, [5]Now at Institute of Radiation Physics, Helmholtz-Zentrum Dresden-Rossendorf e.V., Dresden, Germany, [6]The School of Physics and Astronomy, Centre for Science at Extreme Conditions, and SUPA, University of Edinburgh, Edinburgh, UK, [7]Now at Facility for Open Research in a Compressed Environment, Arizona State University, Tempe, AZ, USA, [8]University Lille, CNRS, INRAE, Centrale Lille, UMR 8207 - UMET - Unité Matériaux et Transformations, Lille, France, [9]Center for Advanced Radiation Sources, The University of Chicago, Chicago, IL, USA, [10]Université Grenoble Alpes, Université Savoie Mont Blanc, CNRS, IRD, IFSTTAR, ISTerre, Grenoble, France, [11]University of Münster, Institut für Mineralogie Corrensstraße 24, Münster, Germany, [12]Institute of Earth and Environmental Sciences, University of Freiburg, Freiburg, Germany, [13]Université Paris Cité, Institut de physique du globe de Paris, CNRS, 1 rue Jussieu, Paris, France, [14]Department of Earth and Planetary Sciences, Jackson School of Geosciences, The University of Texas at Austin, Austin, TX, USA

Key Points:

- We measured thermal conductivity of Fe,Al-bearing bridgmanite, the most abundant mineral in the Earth's lower mantle, up to 85 GPa and 3,100 K
- Finite-element calculations to temperatures obtained from laser flash and X-ray Free Electron Laser heating measurements are fitted to evaluate temperature effect on conductivity
- We assessed pressure, temperature, composition effects on thermal conductivity of bridgmanite at the thermal boundary layer of the lowermost mantle

Supporting Information:

Supporting Information may be found in the online version of this article.

Correspondence to:

R. S. McWilliams and A. F. Goncharov,
R.S.McWilliams@ed.ac.uk;
agoncharov@carnegiescience.edu

Citation:

Edmund, E., Chuvashova, I., Konôpková, Z., Husband, R., Strohm, C., Appel, K., et al. (2024). The thermal conductivity of bridgmanite at lower mantle conditions using a multi-technique approach. *Journal of Geophysical Research: Solid Earth*, *129*, e2024JB028823. https://doi.org/10.1029/2024JB028823

Received 27 JAN 2024
Accepted 27 MAY 2024

Author Contributions:

Conceptualization: Zuzana Konôpková, Cornelius Strohm, Anshuman Mondal, Vitali B. Prakapenka, Zena Younes, Carmen Sanchez-Valle, Hanns-Peter Liermann, James Badro, Jung-Fu Lin, R. Stewart McWilliams, Alexander F. Goncharov
Data curation: Eric Edmund, Irina Chuvashova, Orianna Ball, Victorien Bouffetier, Julien Chantel, Jung-Fu Lin, R. Stewart McWilliams, Alexander F. Goncharov
Formal analysis: Eric Edmund, Irina Chuvashova, Zuzana Konôpková, Rachel Husband, Karen Appel, Carsten Bähtz, Orianna Ball, Kara Brugman, Khachiwan Buakor, Julien Chantel, Stella Chariton,

© 2024. American Geophysical Union. All Rights Reserved.

Abstract The thermal conductivity of bridgmanite, the primary constituent of the Earth's lower mantle, has been investigated using diamond anvil cells at pressures up to 85 GPa and temperatures up to 3,100 K. We report the results of time-domain optical laser flash heating and X-ray Free Electron Laser heating experiments from a variety of bridgmanite samples with different Al and Fe contents. The results demonstrate that Fe or Fe,Al incorporation in bridgmanite reduces thermal conductivity by about 50% in comparison to end-member $MgSiO_3$ at the pressure-temperature conditions of Earth's lower mantle. The effect of temperature on the thermal conductivity at 28–60 GPa is moderate, well described as $k = k_{300}(300/T)^a$, where a is 0.2–0.5. The results yield thermal conductivity of 7.5–15 W/(m × K) in the thermal boundary layer of the lowermost mantle composed of Fe,Al-bearing bridgmanite.

Plain Language Summary Heat transport from the Earth's core and mantle to the surface drives plate tectonics and is crucial for sustaining the magnetic field which shields the surface from the solar wind. To quantify the heat transport process across the core-mantle boundary layer, it is important to know thermal conductivity of major constituent minerals of the lower mantle in the region. Bridgmanite, which was called silicate perovskite, is the most abundant mineral in the lower mantle. Here we measured thermal conductivity on lab-grown bridgmanite with different Fe and Al compositions compressed at the tips of two opposing diamonds to reproduce relevant pressures in the mantle. To obtain thermal conductivity, we applied optical and X-ray Free Electron Lasers combined with optical spectroscopy and X-ray diffraction to heat and measure time-dependent temperature distributions of the sample. Our study provides relevant high pressure-temperature data sets to better constrain the heat flux across the core-mantle boundary.

1. Introduction

Bridgmanite (Bgm) is the most abundant mineral in Earth's lower mantle, comprising upwards of 85% of a pyrolitic lower mantle composition by volume (Mattern et al., 2005). As a result, the thermal conductivity of bridgmanite is the primary control of heat conduction in the bulk lower mantle, while the existence of post-perovskite (Murakami et al., 2004) in the base of the mantle plays a significant role in the heat flux across the core-mantle thermal boundary layer. These in turn substantially influence the thermal evolution and dynamics of

Matthew Duff, Anand Dwivedi, S. M. A. Hosseini-Saber, Torsten Laurus, Xiang Li, Bernhard Masani, James McHardy, Malcolm McMahon, Sébastien Merkel, Katharina Mohrbach, Anshuman Mondal, Guillaume Morard, Vitali B. Prakapenka, Clemens Prescher, Young-Jay Ryu, Jan-Patrick Schwinkendorf, Minxue Tang, Zena Younes, Carmen Sanchez-Valle, James Badro, Jung-Fu Lin, R. Stewart McWilliams, Alexander F. Goncharov
Funding acquisition: Zuzana Konôpková, James McHardy, Malcolm McMahon, Anshuman Mondal, Guillaume Morard, Zena Younes, Carmen Sanchez-Valle, James Badro, Jung-Fu Lin, R. Stewart McWilliams, Alexander F. Goncharov
Investigation: Eric Edmund, Irina Chuvashova, Zuzana Konôpková, Rachel Husband, Cornelius Strohm, Karen Appel, Carsten Bähtz, Orianna Ball, Victorien Bouffetier, Kara Brugman, Khachiwan Buakor, Julien Chantel, Stella Chariton, Matthew Duff, Anand Dwivedi, S. M. A. Hosseini-Saber, Torsten Laurus, Xiang Li, Bernhard Masani, James McHardy, Malcolm McMahon, Sébastien Merkel, Katharina Mohrbach, Anshuman Mondal, Guillaume Morard, Vitali B. Prakapenka, Clemens Prescher, Young-Jay Ryu, Jan-Patrick Schwinkendorf, Minxue Tang, Zena Younes, Carmen Sanchez-Valle, Hanns-Peter Liermann, James Badro, Jung-Fu Lin, R. Stewart McWilliams, Alexander F. Goncharov
Methodology: Irina Chuvashova, Zuzana Konôpková, Rachel Husband, Cornelius Strohm, Karen Appel, Carsten Bähtz, Orianna Ball, Victorien Bouffetier, Kara Brugman, Khachiwan Buakor, Stella Chariton, Matthew Duff, Anand Dwivedi, Konstantin Glazyrin, S. M. A. Hosseini-Saber, Nicolas Jaisle, Bernhard Masani, Malcolm McMahon, Katharina Mohrbach, Guillaume Morard, Vitali B. Prakapenka, Carmen Sanchez-Valle, Hanns-Peter Liermann, James Badro, Jung-Fu Lin, R. Stewart McWilliams, Alexander F. Goncharov
Project administration: Zuzana Konôpková, Rachel Husband, Cornelius Strohm, Zena Younes, Carmen Sanchez-Valle, Jung-Fu Lin, R. Stewart McWilliams, Alexander F. Goncharov
Resources: Zuzana Konôpková, Cornelius Strohm, Karen Appel, Malcolm McMahon, Anshuman Mondal, Guillaume Morard, Zena Younes, Carmen Sanchez-Valle, Hanns-Peter Liermann, James Badro, Jung-Fu Lin, R. Stewart McWilliams, Alexander F. Goncharov
Software: Irina Chuvashova, Zuzana Konôpková, Rachel Husband, Cornelius Strohm, Karen Appel, Carsten Bähtz, Orianna Ball,

the lower mantle temperature from mineral physics and thermodynamic modeling (Garnero & McNamara, 2008; Lay et al., 2008; Tosi et al., 2010). However, the thermal conductivity of Bgm remains poorly understood at the relevant high pressure-temperature conditions of the lower mantle. The results of theoretical calculations using classical and quantum-mechanical methods vary by more than an order of magnitude (from 1 to 14 W/(m*K)) depending on the approach (Ammann et al., 2014; Dekura et al., 2013; Dekura & Tsuchiya, 2019; Ghaderi et al., 2017; Haigis et al., 2012; Stackhouse et al., 2015; Tang et al., 2014; Zhang & Wentzcovitch, 2021). As an additional complication, the major mantle minerals are solid solutions (with various amounts of cations such as Fe, Mg, Al) and have cation disorder, which greatly affects their thermal conductivities (Ohta et al., 2017). This effect has been theoretically estimated in the case of isotopic substitution (Tang & Dong, 2010) but has not been examined thoroughly for large cation disorder in mantle crystals. Experimental investigations of Bgm are scarce and the results are scattered across different compositions (e.g., Fe free) (Hsieh et al., 2017; Ohta et al., 2012), and large discrepancies persist over the effect of composition on the thermal conductivity of bridgmanite (Hsieh et al., 2017; Okuda et al., 2017). In addition, thermal conductivity has been reported to depend on the spin state of Fe^{3+} ion in Fe,Al-bearing crystals (Okuda et al., 2019). Importantly, the lower mantle is subject to high P-T conditions, but the effect of temperature on the thermal conductivity of lower mantle minerals is poorly understood, especially in the case of mixed mantle minerals. The thermal conductivity of candidate mantle minerals typically occurs through phonon scattering mechanisms (Roufosse & Klemens, 1974). However, it is expected to be slower due to a substantial phonon-defect scattering component (Klemens, 1960) in contrast to pure minerals, where one can expect a common phonon-phonon controlled 1/T dependence at high temperatures (Roufosse & Klemens, 1974). As important as it sounds, the temperature effect remains the least explored experimental parameter in our understanding of heat transport in the mantle. This scientific question is a result of our current technical difficulties as combining accurate (e.g., time domain thermoreflectance, TDTR) thermal conductivity measurements with controllable heating to 1,000 s of degrees kelvin is challenging (Hasegawa et al., 2019). Thermal conductivity of Bgm with several Fe and Al composition has been investigated in a large volume press at 26 GPa up to 1,100 K (Manthilake et al., 2011). It was found that thermal conductivity decreases with T following a power law relation with Fe and Fe,Al-bearing Bgm having weaker T dependencies. However, these temperature-scaling relationships are empirical and have not been tested at the direct conditions of the mantle geotherm at approximately 1,800–2,800 K range.

In the present study, the thermal conductivities of end-member $MgSiO_3$, Fe-bearing $MgSiO_3$ and Fe,Al-bearing $MgSiO_3$ are presented from experiments using conventional flash heating at Carnegie Institution for Science (Beck et al., 2007; Konôpková et al., 2016) and a novel X-ray heating method developed at the European X-ray Free Electron Laser (Frost et al., 2024; Liermann et al., 2021; Meza-Galvez et al., 2020). We use these methods to place new constraints on the effect of temperature and composition on the thermal conductivity of Bgm at the conditions of Earth's lower mantle. Our work also encompasses experiments on starting materials with varying crystallinity, showing that poorly crystallized samples exhibit substantially lower thermal conductivity values than well-crystallized counterparts.

2. Materials and Methods

The powdered samples of Bgm for XFEL experiments have been synthesized in the DAC by X-ray and infrared-laser heating of enstatite glass with three Fe-Al composition (Table S1 in Supporting Information S1) at a nominal starting pressure of 35–40 GPa, where crystallization of the samples occurred above 1,800 K. No transmitting medium has been used in the high-pressure chamber. Thin Ir foil sandwiched between slabs of the same glass (in few experiments) was initially intended to be used as a coupler of XFEL and/or infrared laser radiation (Figure S1 in Supporting Information S1); however, all the XFEL experiments reported here involved heating and probing the sample areas free of Ir foil. The densification of the starting enstatite glass typically led to a drop in pressure of about 3–5 GPa. Laser heating of Fe and Fe,Al bearing samples was performed using a 1,064 nm YLF fiber laser (IPG Photonics) at the Earth & Planets Laboratory, Carnegie Institution for Science (Washington, DC). The crystal structure and composition of the synthesized materials have been probed at GSECARS of the Advanced Photon Source (Prakapenka et al., 2008), PETRA III (Liermann et al., 2015), and the European XFEL (EuXFEL) using in situ synchrotron XRD (Figures S2 and S3 in Supporting Information S1).

Single-crystal Bgm samples with 12 mol% Fe and 11 mol% Al (run 5k2179 (Lin et al., 2016)) and 7 mol% Fe (run 5k2174 (Okuchi et al., 2015)) for in-house laser flash experiments were synthesized at 24 GPa and 1,650–1,760°C in a Kawai-type multianvil apparatus (Okuchi et al., 2015); the crystals were the same ones as those used in the

21699356, 2024, 6, Downloaded from https://agupubs.onlinelibrary.wiley.com/doi/10.1029/2024JB028823 by University Of Edinburgh, Wiley Online Library on [17/06/2024]. See the Terms and Conditions (https://onlinelibrary.wiley.com/terms-and-conditions) on Wiley Online Library for rules of use; OA articles are governed by the applicable Creative Commons License

Victorien Bouffetier, Khachiwan Buakor, Stella Chariton, Matthew Duff, Anand Dwivedi, Konstantin Glazyrin, S. M. A. Hosseini-Saber, Nicolas Jaisle, Vitali B. Prakapenka, Carmen Sanchez-Valle, Jung-Fu Lin
Supervision: Cornelius Strohm, James McHardy, Malcolm McMahon, Anshuman Mondal, Guillaume Morard, Zena Younes, Carmen Sanchez-Valle, James Badro, Jung-Fu Lin, R. Stewart McWilliams, Alexander F. Goncharov
Validation: Irina Chuvashova, Zuzana Konôpková, Rachel Husband, Cornelius Strohm, Karen Appel, Carsten Bähtz, Orianna Ball, Victorien Bouffetier, Kara Brugman, Stella Chariton, Matthew Duff, Konstantin Glazyrin, Nicolas Jaisle, Vitali B. Prakapenka, Jung-Fu Lin
Visualization: Eric Edmund, Irina Chuvashova, Vitali B. Prakapenka, Minxue Tang, Jung-Fu Lin, R. Stewart McWilliams, Alexander F. Goncharov
Writing – original draft: Eric Edmund, Jung-Fu Lin, R. Stewart McWilliams, Alexander F. Goncharov
Writing – review & editing: Eric Edmund, Irina Chuvashova, Zuzana Konôpková, Rachel Husband, Cornelius Strohm, Karen Appel, Carsten Bähtz, Orianna Ball, Victorien Bouffetier, Kara Brugman, Khachiwan Buakor, Julien Chantel, Stella Chariton, Matthew Duff, Anand Dwivedi, S. M. A. Hosseini-Saber, Torsten Laurus, Xiang Li, Bernhard Masani, James McHardy, Malcolm McMahon, Sébastien Merkel, Katharina Mohrbach, Anshuman Mondal, Guillaume Morard, Vitali B. Prakapenka, Clemens Prescher, Young-Jay Ryu, Jan-Patrick Schwinkendorf, Minxue Tang, Carmen Sanchez-Valle, Hanns-Peter Liermann, Jung-Fu Lin, R. Stewart McWilliams, Alexander F. Goncharov

previous TDTR study (Hsieh et al., 2017). A number of selected crystals were double-side polished down to 5–8 μm thickness using 3M diamond films. Thin (<300 nm) Ir layers were used as laser energy transducers and have been prepared by pressing between 2 diamond anvils or physical vapor deposition on a glass substrate; these were then positioned on both sides of the sample and the entire sandwich loaded into a DAC cavity with KCl thermal insulation layers between the sandwich and the tips of the diamond anvils.

The symmetric DACs (HIBEF design) for the EuXFEL experiments have been equipped with diamond anvils of 200- and 300-μm culet diameters. One anvil was of standard design mounted on a polycrystalline cubic BN seat; this one was positioned upstream, from which X-ray pulses were delivered. The second anvil of Boehler-Almax design was mounted on a seat with a 60° conical support (Boehler & De Hantsetters, 2004). This geometry provides a larger reciprocal space coverage in XRD experiments using 17.8 keV photons (up to $Q = 5.2$ Å^{-1}), which is critical to better identify and characterize crystallographic changes. The symmetric DACs for in-house laser flash heating experiments were also equipped with diamond anvils with 200- and 300-μm culet diameters mounted on standard tungsten carbide seats.

The XFEL experiments presented here are based on the ability to volumetrically heat low-Z materials by a train of X-ray pulses absorbed by the material (Liermann et al., 2021). The deposited heat sequentially increases the temperature of the bulk of the sample because most of the accumulated heat cannot escape the system between the pulses as the pulse repetition rate is faster than heat transport. Eventually, a steady state is reached; thus, the thermal conductivity of the material is determined by how fast the system reaches the steady state.

The experiments have been performed at the High-Energy Density (HED) Instrument of the EuXFEL in Schenefeld during the 3,160 User Beamtime in September 2022 (Sanchez-Valle, 2022). The repetition rate was set to 4.54 MHz (2.27 MHz in selected experiments); the pulse train contained 200 pulses every 220 or 440 ns resulting in a train duration of 44 or 88 μs, respectively. The X-ray pulse intensity was tuned via absorption filters. The pulse energies with the same train have been usually balanced within <20% deviation. The energies are recorded per pulse using a variety of photodetectors (Liermann et al., 2021) and introduced to finite element (FE) modeling using polynomial fits of temporal variation of raw tabular data. The X-ray beam was focused with a set of Compound Refractive Lenses (CRLs) down to approximately 5 μm in diameter (FWHM) at the sample position, determined from damage imprints measured in freestanding foils. X-ray diffraction is recorded using the high-speed position sensitive Adaptive Gain Integrating Pixel Detector (AGIPD) (Frost et al., 2024), which can record a sequence of individual XRD patterns corresponding to each X-ray pulse in the train.

The X-ray heating in the 10–30 μm thick high-pressure cavity occurs due to a volumetric absorption of very short (<30 fs long) X-ray pulses as described above. The X-ray absorption length of Fe-free Bgm is about 500 μm at 17.8 keV, so the sample, which is much smaller in thickness, absorbs almost uniformly along the X-ray pathway. FE model calculations (Jaisle et al., 2023; Meza-Galvez et al., 2020; Montoya & Goncharov, 2012) (Figures S4 and S5 in Supporting Information S1) have been used to determine the time dependent temperature maps of the high-pressure cavity. The sample temperature has been also measured concomitantly with one-sided streak optical pyrometry (SOP) (Ball et al., 2023; Konôpková et al., 2016), which employs measurements of the time dependent thermal emission spectra using an optical spectrometer coupled to a streak camera. Because the sample is not a strong absorber in the visible to near infrared spectral range (Lobanov et al., 2020), these measurements detect the highest temperature of the sample near the center of the high-pressure cavity. Only temperatures above 2,500 K could be measured because the sample emission is low and due to the strong temperature dependence of the thermal radiation ($\sim T^4$) and a short accumulation time. These measurements can only determine the highest sample temperature at each time. However, rather accurate estimation of the sample temperature variation is needed to determine thermal conductivity; thus, we adopted measurements of the volume thermal expansion as a probe of the time dependent temperature, based on fits of Bgm volume over the duration of the X-ray pulse train. For select temperature series, serial Le Bail refinements of the whole diffraction pattern have been made including >11 resolvable peaks (Figure S3 in Supporting Information S1) and for the remainder of the data set, pseudo-Voigt profiles have been fit to the main (112) reflection of bridgmanite and converted to volume with the assumed unit cell angles. The unit cell geometry is determined by a Le Bail refinement of the first diffraction pattern of the series. It has been reported that Bgm cell geometry is primarily a function of pressure and composition, not temperature (Wolf et al., 2015). In cases where Le Bail refinements and peak fitting have been used independently on the same data set, the differences in volume are negligible (Figure S6 in Supporting Information S1).

21699356, 2024, 6, Downloaded from https://agupubs.onlinelibrary.wiley.com/doi/10.1029/2024JB028823 by University Of Edinburgh, Wiley Online Library on [17/06/2024]. See the Terms and Conditions (https://onlinelibrary.wiley.com/terms-and-conditions) on Wiley Online Library for rules of use; OA articles are governed by the applicable Creative Commons License

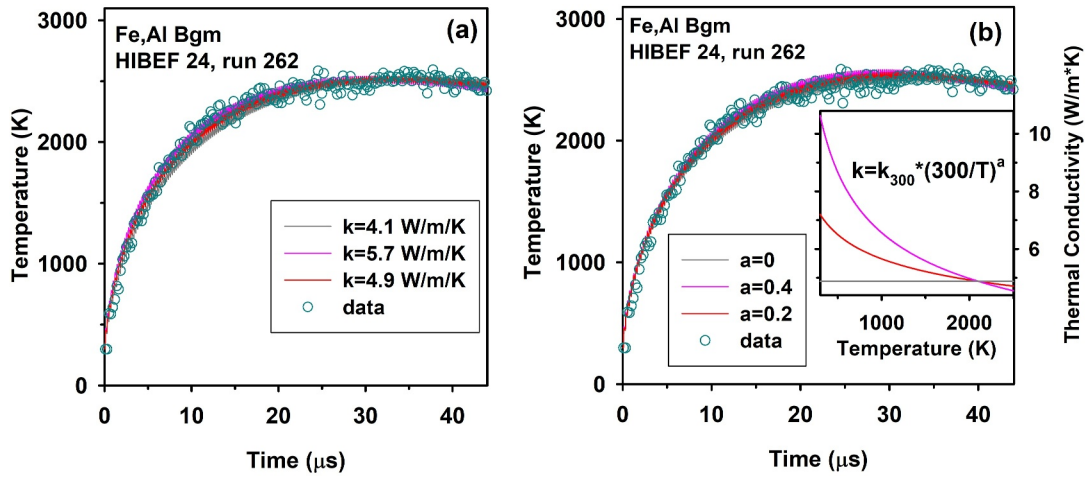

Figure 1. Heating history in the EuXFEL proposal 3,160, run 262, experiment HIBEF 24. Open circles are experimental data. The temperatures are determined using the volume thermal expansion determined in XRD XFEL experiments based on theoretical equation of state and an assumption of 30% of isochoric thermal pressure (Dewaele et al., 1998; Goncharov et al., 2007). The data (circles) are compared to FE calculation in the cavity center (lines) in an assumption of T independent thermal conductivity (a) and T dependent thermal conductivity (b). The inset in (b) shows the model temperature dependencies of thermal conductivity, which were used in FE calculations.

SOP measurements (Figure S7 in Supporting Information S1) were used to validate the temperatures calculated from the thermal expansion model, which will be presented below. The results were consistent within the uncertainties (Figure S8 in Supporting Information S1). Nominal pressures at room temperature have been measured using the spectral position of the Raman peak of the stressed diamond (Akahama & Kawamura, 2006) prior to EuXFEL experiment; these results were consistent with the XRD densities determined at EuXFEL based on experiments and theory of Ref. (Tange et al., 2012).

On the short timescales of individual X-ray pulses (<30 fs), heating is isochoric in the tamped diamond anvil high-pressure cavity. However, during the time interval between the pulses (220–440 ns), there is a relaxation of local thermal pressure, creating a released state via stress waves. Thermal expansion of the heated sample thus occurs prior to the arrival of the next X-ray pulse. The degree of thermal expansion, corrected for any residual thermal pressure resulting from the tamping by the diamond anvils of the high-pressure cavity, determines the temperature via the known high pressure-temperature equation of state. The material state probed by the X-ray pulses likely experiences pressure-temperature (P-T) and stress conditions similar to those in laser heated DAC, which are intermediate to isochoric and isobaric regimes (Meza-Galvez et al., 2020). Previous studies found that P-T conditions in such regimes are well described by assuming that the thermal pressure constitutes 30% of the maximal thermodynamic isochoric pressure $P_{th} \cong 0.3\alpha K_T \Delta T$, where α and K_T are the thermal expansivity and isothermal bulk modulus, and ΔT is the temperature change due to the heating (Dewaele et al., 1998; Goncharov et al., 2007). Temperature in these experiments was determined employing density (ρ), α, and K_T from theoretical calculations (Tange et al., 2012) correcting the density for the atomic substitutions by Fe and Al (Table S1 in Supporting Information S1). Our 2D FE models were fitted to the experimental temperature dependence by refining thermal conductivity. We used the results of the theoretical work (Tange et al., 2012) to calculate the temperature dependent heat capacity c_P and density along the heating P-T pathway required for the models. The sample thickness was estimated using optical interferometry and the experimental refractive index of Bgm scaled to high pressure using the Gladstone-Dale relation (Lobanov et al., 2020). The X-ray absorption coefficient was estimated using the tabulated data (Henke et al., 1993). All parameters including sample thickness, heat capacity, thermal conductivity and assumed EOS, as well as model setup such as thermal pressure approximation and pulse energy variance inclusion, were all tested during modeling to check sensitivity and the effects of the associated uncertainties. We present the parameters of our FE calculations in Table S2 in Supporting Information S1. We performed these calculations with a range of thermal conductivity values and temperature dependences. For each of these calculations, we adjusted the total EuXFEL train energy to find the best match with the experiment thus treating it as a free parameter, with the power on target in the range of 50%–100% of that

21699356, 2024, 6, Downloaded from https://agupubs.onlinelibrary.wiley.com/doi/10.1029/2024JB028823 by University Of Edinburgh, Wiley Online Library on [17/06/2024]. See the Terms and Conditions (https://onlinelibrary.wiley.com/terms-and-conditions) on Wiley Online Library for rules of use; OA articles are governed by the applicable Creative Commons License

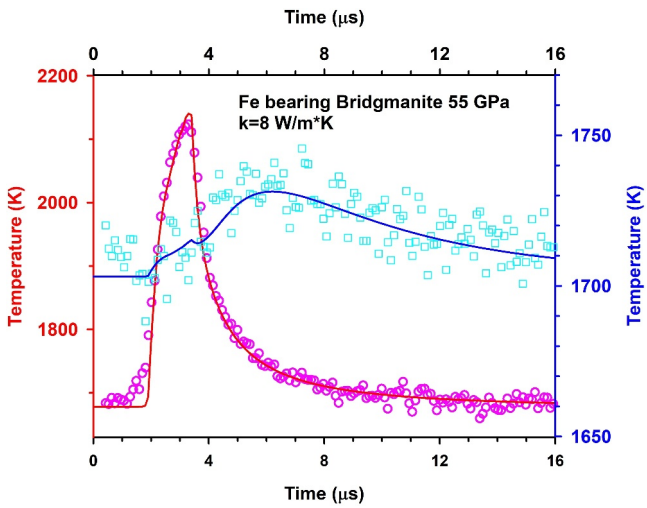

Figure 2. Heating histories in in-house laser flash heating experiment in Fe bearing bridgmanite at 55 GPa. Open circles (pink and cyan symbols correspond to the pulsed heated and the opposite sample sides, respectively) are the experimentally determined radiative temperatures. The solid lines are the fits using best FE calculations (Geballe et al., 2020; Konôpková et al., 2016; Montoya & Goncharov, 2012). The parameters used in the fit are presented in the Table S3 in Supporting Information S1. The model includes about 2% ballistic heating from the opposite sample side due to imperfection of the polarization optics. The first kink upon the temperature rise from the pulsed side, which is not reproduced by the model, is due to streak camera collection imperfections in the vicinity of a strong thermal radiation peak. Please note a change in scale for the temperatures from the pulsed and the opposite sites of the sample.

measured entering the beamline, consistent with contemporaneous performance data for the facility.

The laser flash heating method used for the single-crystal bridgmanite experiments has been described in the previous publications (Geballe et al., 2020; Konôpková et al., 2016; McWilliams et al., 2015). Unlike previous works, the laser pulses creating the heat wave across the sample have been additionally shaped by a Pockels cell producing nearly rectangular pulse shape; this lifts ambiguity in the pulse laser shape and improves the pulse sequence stability. The values of thermal conductivity have been extracted from finite element calculations (Montoya & Goncharov, 2012), where the geometrical parameters of the samples, laser spot diameter are experimentally determined, density and heat capacity are taken from the literature (Tange et al., 2012), while the thermal conductivity and the laser energies are considered as fitting parameters (Table S3 in Supporting Information S1).

3. Results and Discussion

An example of the heating history in one of the experimental XFEL runs is shown in Figure 1. The temperatures have been determined based on the experimental Bgm unit cell volumes (Figure S6 in Supporting Information S1), using the thermal equation of state (Tange et al., 2012) applied along the heating P-T pathway experiencing thermal pressure P_{th} as described above. Our FE calculations fit well the experiment assuming that thermal conductivity is moderately temperature dependent or even constant (Figure 1, Figures S9–S11 in Supporting Information S1). Following the approach used for the experiments in a large volume press at 26 GPa up to 1,000 K (Manthilake et al., 2011), we approximated thermal conductivity of Bgm with the following relation:

$$k_T = k_{300}(300/T)^a, \tag{1}$$

where k_T and k_{300} are the T dependent thermal conductivity and thermal conductivity at 300 K, respectively, and $a = 0.2$–0.43 is a parameter determined for Bgm with each given Fe and Al composition. However, our data are insufficient to accurately determine a; indeed, FE calculations with $a = 0.2 \pm 0.23$ fit well the data (Figure 1). We find that for the best data sets, if fitted with a constant k, the thermal conductivity value corresponds to the values in the high temperature part of the $k(T)$ dependence, where this dependence is moderate (Figure 1b). Therefore, in the cases where we fitted the data with a T independent k, the best fitted value was treated as that determined at high T.

The best fitted results assuming temperature-dependent k following Equation 1 are shown in Figures S9–S11 in Supporting Information S1, and Table S2 of Supplementary Materials shows the parameters used in the fitting procedure. The errors in the values of the extracted thermal conductivities have been estimated based on calculations with a range of temperature independent k and through a comparison of the corresponding temperature histories with the experimental data (Figure 1 and Figures S9–S11 in Supporting Information S1). The error bars are typically within 15% of the value of thermal conductivity at high temperatures, which is comparable to other techniques. The error bars for the thermal conductivity values at 300 K are larger as these are inferred through the temperature dependence of thermal conductivity, which has a large uncertainty in our experiments as discussed above.

The data of the in-house laser flash heating experiments are shown in Figure 2 and Figure S12 in Supporting Information S1. In these experiments the sample is preheated to approximately 1,800 K and thermal conductivity measurements were conducted at this temperature and slightly higher temperatures. Thus, the temperature dependence of thermal conductivity is not captured and only its value at high temperatures (typically 1,700–2,400 K) is measured (Table S3 in Supporting Information S1). The temperature modulation on the heated side of the sample was set to 200–300 K; due to a small thermal conductivity of bridgmanite, the temperature variation on

21699356, 2024, 6, Downloaded from https://agupubs.onlinelibrary.wiley.com/doi/10.1029/2024JB028823 by University Of Edinburgh, Wiley Online Library on [17/06/2024]. See the Terms and Conditions (https://onlinelibrary.wiley.com/terms-and-conditions) on Wiley Online Library for rules of use; OA articles are governed by the applicable Creative Commons License

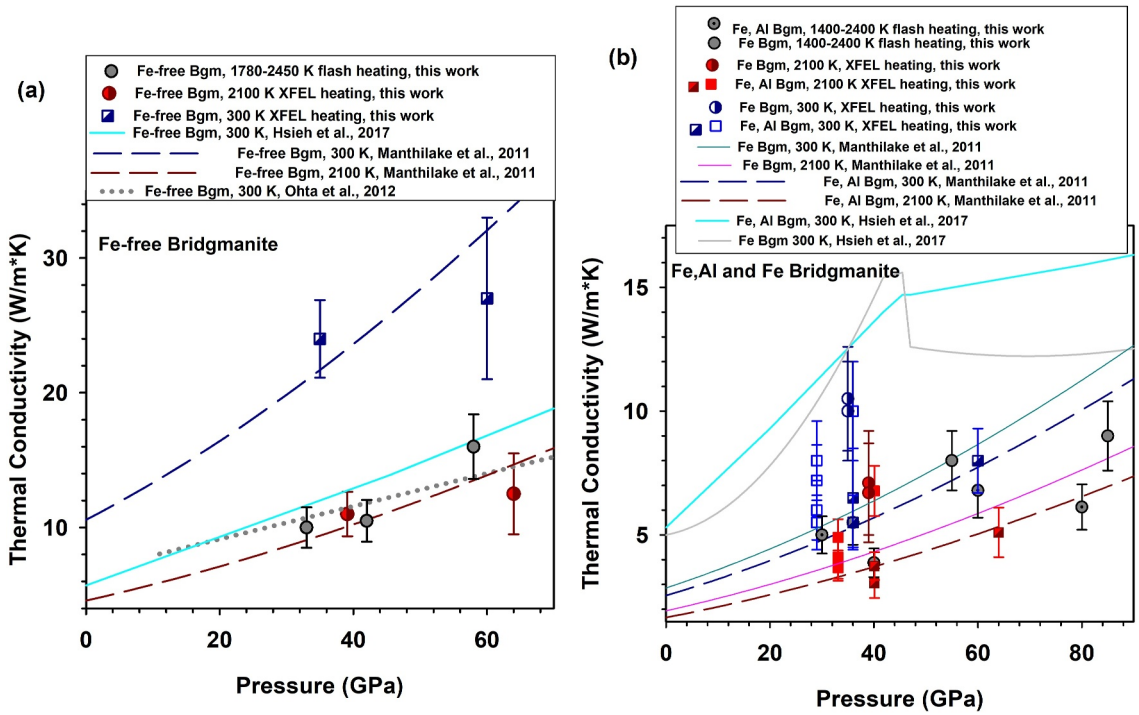

Figure 3. Thermal conductivity of Fe-free (a) Fe,Al and Fe-bearing (b) Bgm as a function of pressure at high temperatures and room temperature. Symbols correspond to the results of this work determined in XFEL and in-house laser flash experiments. Semi-filled symbols correspond to XFEL experiments where Bgm samples were crystallized in the XFEL beam, while open and filled squares correspond to the experiments where Bgm was crystallized by laser heating. Various lines correspond to previously reported experiments (Hsieh et al., 2017; Ohta et al., 2012) at 300 K and at 300 and 2,100 K deduced from the model presented in Ref. (Manthilake et al., 2011).

the opposite side is about 10–20 K and this temperature peak is delayed by several microseconds. This allows us to constrain the thermal resistance of the Ir-Bgm-Ir sandwich in the finite-element models. The value of thermal conductivity of the Ir heat/radiation transducers from both sides of the sample is difficult to determine as it does not clearly correlate with any feature in the observations; thus, thermal conductivity of Ir was assumed to be close to that at ambient pressure.

Figure 3 presents the thermal conductivity values as a function of pressure determined for Fe,Al-free (a) and Fe,Al and Fe-bearing Bgm (b) at high (1,750–3,100 K) and room temperatures. The data determined by different techniques (XFEL vs. flash heating) are generally consistent even though the values are somewhat scattered. It is important to note that XFEL thermal conductivity values presented here for Fe and Fe,Al bearing Bgm are from measurements carried out on material that was pre-crystallized offline using continuous laser heating. This results in more extensive grain growth in the heated spot, as well as producing a larger crystallized area thanks to the use of a laser-heating system with larger beam dimensions than that of the XFEL X-ray beam (~10 vs. ~3 μm), as well as different heating timescales (minutes vs. 10 s of microseconds). This is visually corroborated by the relative sizes of crystallized areas produced by XFEL and LH heating (Figure S1 in Supporting Information S1). Some experiments have been carried out on the same samples, at the same pressures, where Bgm has been crystallized directly in the XFEL X-ray beam. In this case, the thermal conductivity value is always systematically lower (Table S2 in Supporting Information S1), with smaller temperature dependence, likely reflecting the significant influence of grain size effects or residual glass on the effective thermal conductivity of the probed sample region. This highlights the need to have well-crystallized, annealed starting materials to produce accurate thermal conductivity values in these novel experiments.

The values of thermal conductivity are approximately two times larger for Fe,Al- free bridgmanite compared to Fe,Al and Fe bearing Bgm. The results for $MgSiO_3$ are in a good agreement with theoretical calculations of Refs. (Dekura & Tsuchiya, 2019; Ghaderi et al., 2017; Zhang & Wentzcovitch, 2021). This result is also in good agreement with previous multi-anvil studies (Manthilake et al., 2011), but it is at odds with more recent DAC

21699356, 2024, 6, Downloaded from https://agupubs.onlinelibrary.wiley.com/doi/10.1029/2024JB028823 by University Of Edinburgh, Wiley Online Library on [17/06/2024]. See the Terms and Conditions (https://onlinelibrary.wiley.com/terms-and-conditions) on Wiley Online Library for rules of use; OA articles are governed by the applicable Creative Commons License

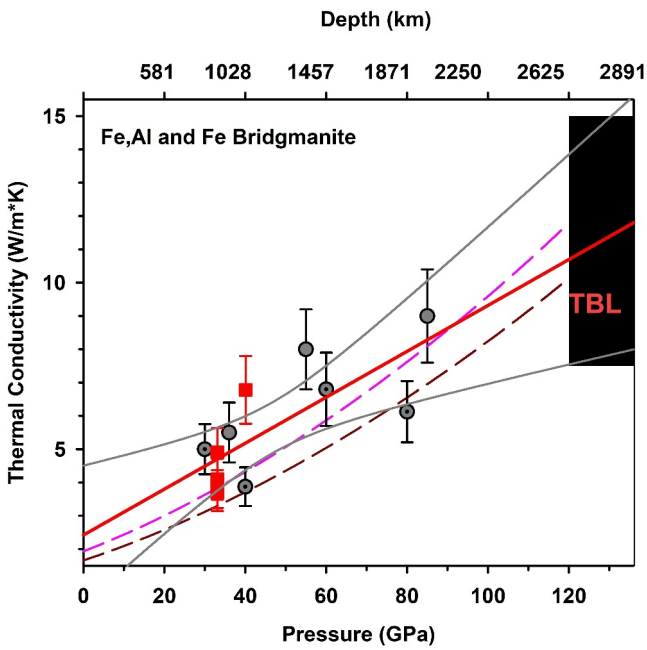

Figure 4. Thermal conductivity of Fe,Al and Fe-bearing Bgm as a function of pressure at high temperatures (2,100 K). Black circles with gray filling correspond to in-house laser flash experiments (dotted- Fe,Al and plain- Fe bearing Bgm, respectively) and red filled squares correspond to XFEL experiments where Fe,Al Bgm was crystallized by prior laser heating. The solid red line is the linear fit to all data and the solid gray lines correspond to 95% confidence intervals. Dashed lines are thermodynamic models from Ref. (Manthilake et al., 2011). Black rectangle corresponds to the best values of thermal conductivity of Fe,Al and Fe-bearing Bgm of this work at the pressure conditions of the thermal boundary layer in the base of the lower mantle.

TDTR measurements (Hsieh et al., 2017), which show very similar values for all Fe, Al compositions below 44 GPa. Our values of thermal conductivity at 300 K are larger than those of Ref. (Hsieh et al., 2017) for Fe-free Bgm, but are smaller for Fe and Fe,Al- bearing Bgm. Our data at 300 K for $MgSiO_3$ are also in odd with the 2 ns TDTR measurements of Ref. (Ohta et al., 2012). These discrepancies with previous TDTR measurements (Hsieh et al., 2017; Ohta et al., 2012) are curious, given that the same batch of Bgm crystals were used in our study at high P-T conditions and in a previous TDTR study at high P and room T (Hsieh et al., 2017). One explanation (which cannot account for all discrepanies) could be that TDTR experiments were performed at essentially room temperature, while in this work the results are based on the high-temperature experiments and room-temperature results are inferred. However, our results agree with Ref. (Manthilake et al., 2011) concerning the values and general tendencies even though the results of these studies are model extrapolations to various P-T conditions based on measurements at one pressure point. The thermal conductivity values determined here for Fe-bearing and Fe,Al-bearing Bgm at high P-T conditions are in agreement with the extrapolations of Ref. (Manthilake et al., 2011), albeit scattered.

The pressure dependencies of thermal conductivity of Bgm with different composition and at different temperatures show an increase in the value with pressure, but the pressure slope is difficult to determine accurately and systematically because the data are fragmentary, and they scatter. Based on the data presented here, omitting data for poorly crystallized samples in XFEL experiments, the thermal conductivity of Fe and Fe,Al bearing Bgm along the mantle geotherm varies from 4(1) W/m/K at the top of the uppermost lower mantle to 11(4) W/m/K when extrapolated to the base of the lower mantle at ambient mantle temperatures (Figure 4). This result provides direct evidence that the thermal conductivity of Bgm is enhanced at deep lower mantle conditions, therefore reducing convective flow and possibly aiding to stabilize thermochemical heterogeneities in the deep lower mantle (Arnould et al., 2020; Garnero & McNamara, 2008).

The assessed here pressure and temperature tendencies of the thermal conductivity of Bgm support the models using thermodynamic scaling relations (Dalton et al., 2013; Manthilake et al., 2011), which are based on the Debye-Grüneisen theory. More dense and accurate data are needed to establish the temperature and pressure dependencies of thermal conductivity at high pressures and high temperatures including a possible suppression of thermal conductivity of Fe and Fe,Al bearing Bgm above 45 GPa (Hsieh et al., 2017), which cannot be ruled out based on the data of this work. This latter scenario agrees better with the previous laser flash experiments with synthetic samples produced from pyrolite glass (Geballe et al., 2020). Thus, further studies are needed to clarify the temperature-dependence of bridgmanite thermal conductivity at the P-T conditions of the lower mantle.

4. Conclusions

Our experiments determined the values of thermal conductivity of Bgm samples with a range of compositions and grain sizes at high to room temperatures and pressures up to 80 GPa. The results constrain thermal conductivity of Bgm with various Fe,Al composition at relevant P-T conditions of the lower mantle up to 85 GPa at 1,450–2,450 K (flash heating experiments) and of Fe and Fe,Al-bearing Bgm up to 60 GPa and 3,100 K (XFEL experiments). The most reliable data indicate that the thermal conductivity increases in the deep lower mantle, thus suggesting a reduced convective flow aiding to stabilize thermochemical heterogeneities in the deep mantle. Even though the value of thermal conductivity at the P-T conditions of the thermal boundary layer (2,500–4,000 K, 120–136 GPa) has a large uncertainty, the results determined at relevant temperatures are valuable as previous determinations inferred these quantities using scaling relations (Dalton et al., 2013; Hsieh et al., 2017; Manthilake et al., 2011; Ohta et al., 2012). The best determined value of the thermal conductivity of Bgm at the bottom of the thermal boundary layer (7.5–15 W/(m*K)) provides a new reliable constraint, which is larger than previously reported (Geballe et al., 2020; Hsieh et al., 2017; Tang et al., 2014) but in agreement with theory of (Stackhouse

21699356, 2024, 6, Downloaded from https://agupubs.onlinelibrary.wiley.com/doi/10.1029/2024JB028823 by University Of Edinburgh, Wiley Online Library on [17/06/2024]. See the Terms and Conditions (https://onlinelibrary.wiley.com/terms-and-conditions) on Wiley Online Library for rules of use; OA articles are governed by the applicable Creative Commons License

et al., 2015). This makes the best CMB heat flux estimation in the 10–20 TW range (Tang et al., 2014), in broad agreement with recent geophysical estimations (Nimmo, 2015).

Data Availability Statement

The data sets used in this paper are available in Supplementary Materials and at Sanchez-Valle (2022).

Acknowledgments
The authors are indebted to the HIBEF user consortium for the provision of instrumentation and staff that enabled this experiment. We acknowledge European XFEL in Schenefeld, Germany, for provision of X-ray free-electron laser beamtime at Scientific Instrument HED (High Energy Density Science) and would like to thank the staff for their assistance. We acknowledge DESY (Hamburg, Germany), a member of the Helmholtz Association HGF, for the provision of experimental facilities. Parts of this research were carried out at PETRA III (beamline P02.2). Parts of this research were carried out at the GeoSoilEnviroCARS (The University of Chicago, Sector 13), Advanced Photon Source (Argonne National Laboratory). GeoSoilEnviroCARS is supported by the National Science Foundation—Earth Sciences (EAR-1634415). E. E. and A.F. G. acknowledge support of the US National Science Foundation Grant EAR-2049127 and Carnegie Science. A.F.G. acknowledges support of the National Science Foundation Grant DMR-2200670 and Carnegie Canada. G.M. and N.J. were financed by IDEX Université Grenoble Alpes, by a grant from Labex OSUG@2,020 (Investissements d'avenir —ANR10 LABX56) and by the Programme National de Planetologie (PNP) of CNRS/INSU. Karen Appel and Khachiwan Buakor acknowledge the DFG for financial support via AP262/2-2. JFL acknowledges support from the NSF Geophysics Program (EAR-2001381). J.B. acknowledges funding from the European Research Council (ERC) under the European Union's Horizon 2020 research and innovation program (Grant 101019965), and support of LabEx UnivEarthS, ANR-10-LABX-0023 and ANR-18-IDEX-0001, by IPGP multidisciplinary program PARI and by Paris–IdF region SESAME Grant 12015908.

References

Akahama, Y., & Kawamura, H. (2006). Pressure calibration of diamond anvil Raman gauge to 310GPa. *Journal of Applied Physics*, *100*(4), 043516. https://doi.org/10.1063/1.2335683

Ammann, M. W., Walker, A. M., Stackhouse, S., Wookey, J., Forte, A. M., Brodholt, J. P., & Dobson, D. P. (2014). Variation of thermal conductivity and heat flux at the Earth's core mantle boundary. *Earth and Planetary Science Letters*, *390*, 175–185. https://doi.org/10.1016/j.epsl.2014.01.009

Arnould, M., Coltice, N., Flament, N., & Mallard, C. (2020). Plate tectonics and mantle controls on plume dynamics. *Earth and Planetary Science Letters*, *547*, 116439. https://doi.org/10.1016/j.epsl.2020.116439

Ball, O. B., Prescher, C., Appel, K., Baehtz, C., Baron, M. A., Briggs, R., et al. (2023). Dynamic optical spectroscopy and pyrometry of static targets under optical and x-ray laser heating at the European XFEL. *Journal of Applied Physics*, *134*(5). https://doi.org/10.1063/5.0142196

Beck, P., Goncharov, A. F., Struzhkin, V. V., Militzer, B., Mao, H. K., & Hemley, R. J. (2007). Measurement of thermal diffusivity at high pressure using a transient heating technique. *Applied Physics Letters*, *91*(18), 181914. https://doi.org/10.1063/1.2799243

Boehler, R., & De Hantsetters, K. (2004). New anvil designs in diamond-cells. *High Pressure Research*, *24*(3), 391–396. https://doi.org/10.1080/08957950412331323924

Dalton, D. A., Hsieh, W.-P., Hohensee, G. T., Cahill, D. G., & Goncharov, A. F. (2013). Effect of mass disorder on the lattice thermal conductivity of MgO periclase under pressure: Implication for the deep Earth heat flow. *Scientific Reports*, *3*(1), 2400. https://doi.org/10.1038/srep02400

Dekura, H., & Tsuchiya, T. (2019). Lattice Thermal Conductivity of MgSiO3 Postperovskite Under the Lowermost Mantle Conditions from Ab Initio Anharmonic Lattice Dynamics. *Geophysical Research Letters*, *46*(22), 12919–12926. https://doi.org/10.1029/2019gl085273

Dekura, H., Tsuchiya, T., & Tsuchiya, J. (2013). Ab initio lattice Thermal Conductivity of MgSiO3 Perovskite as Found In Earth's Lower mantle. *Physical Review Letters*, *110*(2), 025904. https://doi.org/10.1103/physrevlett.110.025904

Dewaele, A., Fiquet, G., & Gillet, P. (1998). Temperature and pressure distribution in the laser-heated diamond–anvil cell. *Review of Scientific Instruments*, *69*(6), 2421–2426. https://doi.org/10.1063/1.1148970

Frost, M., McWilliams, R. S., Bykova, E., Bykov, M., Husband, R. J., Andriambariarijaona, L. M., et al. (2024). Diamond precipitation dynamics from hydrocarbons at icy planet interior conditions. *Nature Astronomy*, *8*(2), 174–181. https://doi.org/10.1038/s41550-023-02147-x

Garnero, E. J., & McNamara, A. K. (2008). Structure and dynamics of Earth's lower mantle. *Science*, *320*(5876), 626–628. https://doi.org/10.1126/science.1148028

Geballe, Z. M., Sime, N., Badro, J., van Keken, P. E., & Goncharov, A. F. (2020). Thermal conductivity near the bottom of the Earth's lower mantle: Measurements of pyrolite up to 120 GPa and 2500 K. *Earth and Planetary Science Letters*, *536*, 116161. https://doi.org/10.1016/j.epsl.2020.116161

Ghaderi, N., Zhang, D.-B., Zhang, H., Xian, J., Wentzcovitch, R. M., & Sun, T. (2017). Lattice thermal conductivity of MgSiO3 perovskite from first principles. *Scientific Reports*, *7*(1), 5417. https://doi.org/10.1038/s41598-017-05523-6

Goncharov, A. F., Crowhurst, J. C., Dewhurst, J. K., Sharma, S., Sanloup, C., Gregoryanz, E., et al. (2007). Thermal equation of state of cubic boron nitride: Implications for a high-temperature pressure scale. *Physical Review B*, *75*(22), 224114. https://doi.org/10.1103/physrevb.75.224114

Haigis, V., Salanne, M., & Jahn, S. (2012). Thermal conductivity of MgO, MgSiO 3 perovskite and post-perovskite in the Earth's deep mantle. *Earth and Planetary Science Letters*, *355*, 102–108. https://doi.org/10.1016/j.epsl.2012.09.002

Hasegawa, A., Yagi, T., & Ohta, K. (2019). Combination of pulsed light heating thermoreflectance and laser-heated diamond anvil cell for in-situ high pressure-temperature thermal diffusivity measurements. *Review of Scientific Instruments*, *90*(7), 074901. https://doi.org/10.1063/1.5093343

Henke, B. L., Gullikson, E. M., & Davis, J. C. (1993). X-Ray interactions: Photoabsorption, scattering, transmission, and reflection at E = 50-30,000 eV, Z = 1-92. *Atomic Data and Nuclear Data Tables*, *54*(2), 181–342. https://doi.org/10.1006/adnd.1993.1013

Hsieh, W.-P., Deschamps, F., Okuchi, T., & Lin, J.-F. (2017). Reduced lattice thermal conductivity of Fe-bearing bridgmanite in Earth's deep mantle. *Journal of Geophysical Research: Solid Earth*, *122*(7), 4900–4917. https://doi.org/10.1002/2017jb014339

Jaisle, N., Cébron, D., Konôpková, Z., Husband, R. J., Prescher, C., Cerantola, V., et al. (2023). MHz free electron laser x-ray diffraction and modeling of pulsed laser heated diamond anvil cell. *Journal of Applied Physics*, *134*(9). https://doi.org/10.1063/5.0149836

Klemens, P. G. (1960). Thermal resistance due to point defects at high temperatures. *Physical Review*, *119*(2), 507–509. https://doi.org/10.1103/physrev.119.507

Konôpková, Z., McWilliams, R. S., Gómez-Pérez, N., & Goncharov, A. F. (2016). Direct measurement of thermal conductivity in solid iron at planetary core conditions. *Nature*, *534*(7605), 99–101. https://doi.org/10.1038/nature18009

Lay, T., Hernlund, J., & Buffett, B. A. (2008). Core-mantle boundary heat flow. *Nature Geoscience*, *1*, 25–32. https://doi.org/10.1038/ngeo.2007.44

Liermann, H. P., Konopkova, Z., Appel, K., Prescher, C., Schropp, A., Cerantola, V., et al. (2021). Novel experimental setup for megahertz X-ray diffraction in a diamond anvil cell at the High Energy Density (HED) instrument of the European X-ray Free-Electron Laser (EuXFEL). *Journal of Synchrotron Radiation*, *28*(3), 688–706. https://doi.org/10.1107/s1600577521002551

Liermann, H.-P., Konopkova, Z., Morgenroth, W., Glazyrin, K., Bednarcik, J., McBride, E. E., et al. (2015). The extreme conditions beamline P02.2 and the extreme conditions science infrastructure at PETRA III. *Journal of Synchrotron Radiation*, *22*(4), 908–924. https://doi.org/10.1107/s1600577515005937

Lin, J.-F., Mao, Z., Yang, J., Liu, J., Xiao, Y., Chow, P., & Okuchi, T. (2016). High-spin Fe2+ and Fe3+ in single-crystal aluminous bridgmanite in the lower mantle. *Geophysical Research Letters*, *43*(13), 6952–6959. https://doi.org/10.1002/2016gl069836

Lobanov, S. S., Holtgrewe, N., Ito, G., Badro, J., Piet, H., Nabiei, F., et al. (2020). Blocked radiative heat transport in the hot pyrolitic lower mantle. *Earth and Planetary Science Letters*, *537*, 116176. https://doi.org/10.1016/j.epsl.2020.116176

21699356, 2024, 6, Downloaded from https://agupubs.onlinelibrary.wiley.com/doi/10.1029/2024JB028823 by University Of Edinburgh, Wiley Online Library on [17/06/2024]. See the Terms and Conditions (https://onlinelibrary.wiley.com/terms-and-conditions) on Wiley Online Library for rules of use; OA articles are governed by the applicable Creative Commons License

Manthilake, G. M., de Koker, N., Frost, D. J., & McCammon, C. A. (2011). Lattice thermal conductivity of lower mantle minerals and heat flux from Earth's core. *Proceedings of the National Academy of Sciences*, *108*(44), 17901–17904. https://doi.org/10.1073/pnas.1110594108

Mattern, E., Matas, J., Ricard, Y., & Bass, J. (2005). Lower mantle composition and temperature from mineral physics and thermodynamic modelling. *Geophysical Journal International*, *160*(3), 973–990. https://doi.org/10.1111/j.1365-246x.2004.02549.x

McWilliams, R. S., Konôpková, Z., & Goncharov, A. F. (2015). A flash heating method for measuring thermal conductivity at high pressure and temperature: Application to Pt. *Physics of the Earth and Planetary Interiors*, *247*, 17–26. https://doi.org/10.1016/j.pepi.2015.06.002

Meza-Galvez, J., Gomez-Perez, N., Marshall, A. S., Coleman, A. L., Appel, K., Liermann, H. P., et al. (2020). Thermomechanical response of thickly tamped targets and diamond anvil cells under pulsed hard x-ray irradiation. *Journal of Applied Physics*, *127*(19). https://doi.org/10.1063/1.5141360

Montoya, J. A., & Goncharov, A. F. (2012). Finite element calculations of the time dependent thermal fluxes in the laser-heated diamond anvil cell. *Journal of Applied Physics*, *111*(11), 112617. https://doi.org/10.1063/1.4726231

Murakami, M., Hirose, K., Kawamura, K., Sata, N., & Ohishi, Y. (2004). Post-perovskite phase transition in MgSiO3. *Science*, *304*(5672), 855–858. https://doi.org/10.1126/science.1095932

Nimmo, F. (2015). 8.02 - energetics of the core. In G. Schubert (Ed.), *Treatise on Geophysics* (2nd ed., pp. 27–55). Elsevier.

Ohta, K., Yagi, T., Hirose, K., & Ohishi, Y. (2017). Thermal conductivity of ferropericlase in the Earth's lower mantle. *Earth and Planetary Science Letters*, *465*, 29–37. https://doi.org/10.1016/j.epsl.2017.02.030

Ohta, K., Yagi, T., Taketoshi, N., Hirose, K., Komabayashi, T., Baba, T., et al. (2012). Lattice thermal conductivity of MgSiO3 perovskite and post-perovskite at the core–mantle boundary. *Earth and Planetary Science Letters*, *349*, 109–115. https://doi.org/10.1016/j.epsl.2012.06.043

Okuchi, T., Purevjav, N., Tomioka, N., Lin, J.-F., Kuribayashi, T., Schoneveld, L., et al. (2015). Synthesis of large and homogeneous single crystals of water-bearing minerals by slow cooling at deep-mantle pressures. *American Mineralogist*, *100*(7), 1483–1492. https://doi.org/10.2138/am-2015-5237

Okuda, Y., Ohta, K., Sinmyo, R., Hirose, K., Yagi, T., & Ohishi, Y. (2019). Effect of spin transition of iron on the thermal conductivity of (Fe, Al)-bearing bridgmanite. *Earth and Planetary Science Letters*, *520*, 188–198. https://doi.org/10.1016/j.epsl.2019.05.042

Okuda, Y., Ohta, K., Yagi, T., Sinmyo, R., Wakamatsu, T., Hirose, K., & Ohishi, Y. (2017). The effect of iron and aluminum incorporation on lattice thermal conductivity of bridgmanite at the Earth's lower mantle. *Earth and Planetary Science Letters*, *474*, 25–31. https://doi.org/10.1016/j.epsl.2017.06.022

Prakapenka, V. B., Kubo, A., Kuznetsov, A., Laskin, A., Shkurikhin, O., Dera, P., et al. (2008). Advanced flat top laser heating system for high pressure research at GSECARS: Application to the melting behavior of germanium. *High Pressure Research*, *28*(3), 225–235. https://doi.org/10.1080/08957950802050718

Roufosse, M. C., & Klemens, P. G. (1974). Lattice thermal conductivity of minerals at high temperatures. *Journal of Geophysical Research*, *79*(5), 703–705. https://doi.org/10.1029/jb079i005p00703

Sanchez-Valle, C. (2022). Thermal conductivity of insulators in deep planetary interiors [Dataset]. *Proposal no. 003160. European XFEL*. https://in.xfel.eu/metadata/doi/10.22003/XFEL.EU-DATA-003160-00

Stackhouse, S., Stixrude, L., & Karki, B. B. (2015). First-principles calculations of the lattice thermal conductivity of the lower mantle. *Earth and Planetary Science Letters*, *427*, 11–17. https://doi.org/10.1016/j.epsl.2015.06.050

Tang, X., & Dong, J. (2010). Lattice thermal conductivity of MgO at conditions of Earth's interior. *Proceedings of the National Academy of Sciences*, *107*(10), 4539–4543. https://doi.org/10.1073/pnas.0907194107

Tang, X., Ntam, M. C., Dong, J., Rainey, E. S. G., & Kavner, A. (2014). The thermal conductivity of Earth's lower mantle. *Geophysical Research Letters*, *41*(8), 2746–2752. https://doi.org/10.1002/2014gl059385

Tange, Y., Kuwayama, Y., Irifune, T., Funakoshi, K.-i., & Ohishi, Y. (2012). P-V-T equation of state of MgSiO3 perovskite based on the MgO pressure scale: A comprehensive reference for mineralogy of the lower mantle. *Journal of Geophysical Research*, *117*(B6), B06201. https://doi.org/10.1029/2011jb008988

Tosi, N., Yuen, D. A., & Čadek, O. (2010). Dynamical consequences in the lower mantle with the post-perovskite phase change and strongly depth-dependent thermodynamic and transport properties. *Earth and Planetary Science Letters*, *298*(1–2), 229–243. https://doi.org/10.1016/j.epsl.2010.08.001

Wolf, A. S., Jackson, J. M., Dera, P., & Prakapenka, V. B. (2015). The thermal equation of state of (Mg, Fe)SiO3 bridgmanite (perovskite) and implications for lower mantle structures. *Journal of Geophysical Research: Solid Earth*, *120*(11), 7460–7489. https://doi.org/10.1002/2015jb012108

Zhang, Z., & Wentzcovitch, R. M. (2021). Ab initio lattice thermal conductivity of $MgSiO_3$ across the perovskite-postperovskite phase transition. *Physical Review B*, *103*(14), 144103. https://doi.org/10.1103/physrevb.103.144103

21699356, 2024, 6, Downloaded from https://agupubs.onlinelibrary.wiley.com/doi/10.1029/2024JB028823 by University Of Edinburgh, Wiley Online Library on [17/06/2024]. See the Terms and Conditions (https://onlinelibrary.wiley.com/terms-and-conditions) on Wiley Online Library for rules of use; OA articles are governed by the applicable Creative Commons License